Cellular and Molecular Life Sciences (2023) 80:302
https://doi.org/10.1007/s00018-023-04962-x

ORIGINAL ARTICLE

Metabolic and cell cycle shift induced by the deletion of *Dnm1l* attenuates the dissolution of pluripotency in mouse embryonic stem cells

Bong Jong Seo[1] · Seung Bin Na[1] · Joonhyuk Choi[1] · Byeongyong Ahn[1] · Omer Habib[2] · Chankyu Park[1] · Kwonho Hong[1] · Jeong Tae Do[1]

Received: 20 April 2023 / Revised: 12 September 2023 / Accepted: 12 September 2023 / Published online: 25 September 2023

Abstract

Mitochondria are versatile organelles that continuously change their morphology via fission and fusion. However, the detailed functions of mitochondrial dynamics-related genes in pluripotent stem cells remain largely unclear. Here, we aimed to determine the effects on energy metabolism and differentiation ability of mouse embryonic stem cells (ESCs) following deletion of the mitochondrial fission-related gene *Dnm1l*. Resultant *Dnm1l*$^{-/-}$ ESCs maintained major pluripotency characteristics. However, *Dnm1l*$^{-/-}$ ESCs showed several phenotypic changes, including the inhibition of differentiation ability (dissolution of pluripotency). Notably, *Dnm1l*$^{-/-}$ ESCs maintained the expression of the pluripotency marker Oct4 and undifferentiated colony types upon differentiation induction. RNA sequencing analysis revealed that the most frequently differentially expressed genes were enriched in the glutathione metabolic pathway. Our data suggested that differentiation inhibition of *Dnm1l*$^{-/-}$ ESCs was primarily due to metabolic shift from glycolysis to OXPHOS, G2/M phase retardation, and high level of *Nanog* and 2-cell-specific gene expression.

Keywords Dynamin 1 like (Dnm1l) · Embryonic stem cells (ESCs) · Mitochondrial fission · Pluripotency · Cellular metabolism

Introduction

Mitochondria are versatile organelles with a variety of functions and can self-divide or change their morphology via fission and fusion. Mitochondrial fission and fusion occur dynamically in response to the cellular environment and, thus, are crucial for cellular function and survival [5, 29]. Accordingly, the number of mitochondria and their functions are influenced by mitochondrial biogenesis (division) and mitochondrial dynamics (fission and fusion) [41]. Several proteins are involved in the mitochondrial fission and fusion processes in eukaryotes [61]. In mammals, Mfn1/2 (mitofusin 1/2) and Opa1 (optic atrophy 1) are located in the outer and inner membranes, respectively, and regulate mitochondrial fusion. Dnm1l (dynamin 1-like), Fis1 (fission, mitochondrial 1), and Mff (mitochondrial fission factor) are located in the mitochondrial outer membrane and regulate mitochondrial fission [58, 61].

Pluripotent stem cells (PSCs), such as embryonic stem cells (ESCs) and induced pluripotent stem cells (iPSCs), represent the early developmental state, viz. the inner cell mass of the blastocyst [12]. These PSCs have great potential for research in various fields and for clinical approaches owing to their self-renewal ability and potential to differentiate into all three germ layers [63]. Mitochondrial function is closely associated with the self-renewal and differentiation abilities of PSCs [16, 17, 28, 49, 68, 70]. In general, adult somatic cells obtain energy, adenosine triphosphate (ATP), from aerobic metabolism based on oxidative phosphorylation (OXPHOS). Alternatively, PSCs are heavily dependent on anaerobic glycolysis; this may be correlated with mitochondrial shape and the number of mitochondria in the cytoplasm [17, 26]. Mitochondrial morphologies vary

✉ Jeong Tae Do
dojt@konkuk.ac.kr

[1] Department of Stem Cell and Regenerative Biotechnology, Konkuk Institute of Technology, Konkuk University, Seoul 05029, Republic of Korea

[2] Department of Chemistry, Hanyang University, Seoul 04763, Republic of Korea

depending on cell types. Differentiated cells generally possess elongated and branched, rod-shaped mitochondria with well-developed cristae, and a denser matrix. PSCs possess globular-shaped mitochondria with poorly developed cristae and a loose matrix compared with differentiated cells [8, 13, 14]. Furthermore, it has been reported that specific mitochondrial features, such as morphology, localization, and number, are crucial factors for maintaining pluripotency and cellular differentiation [30].

One of the main effector proteins associated with mitochondrial fission is Dnm1l (DRP1 in humans), which functions as a GTPase [4]. Cytosolic Dnm1l proteins are recruited to the mitochondrial outer membrane and form multiple helical complexes to conduct mitochondrial fission by constricting the mitochondria [15]. Loss of *Dnm1l* results in embryonic lethality as early as embryonic day (E) 11.5 [59], indicating the importance of Dnm1l in normal embryonic development and survival. Moreover, studies using knockout mouse models suggested that Dnm1l plays a critical role in the normal functioning of tissues such as the brain [21, 59] and heart [50]. These results were consistent with the observation in humans that the mitochondrial fission protein DRP1 is essential for neuronal function [40] and is involved in various types of cardiovascular diseases [35]. However, the detailed mechanism and etiology of Dnm1l for diseases and embryonic development have not yet been elucidated. Ishihara et al. reported that *Dnm1l* knockout ($Dnm1l^{-/-}$) ESCs and fibroblasts grow slightly slower than their control counterparts [21]. In addition, Dnm1l protein levels are correlated with cyclin-Cdk complexes and, thus, may be involved in cell cycle transition [47]. The GTPase activity of Dnm1l is directly regulated by cyclin B-Cdk1 complexes and leads to mitochondrial fission during the G2/M cell cycle transition [51]. Therefore, a deficiency of the Dnm1l protein causes G2/M cell cycle retardation [43]. Although there have been several reports regarding the association between Dnm1l and the cell cycle, further studies on different cell types and cell conditions are necessary to understand the correlation between mitochondrial dynamics and metabolism and the cell cycle. Notably, knockout effects of the mitochondrial fission gene *Dnm1l* have been poorly reported in mouse ESCs. Recently, we reported that knockout of mitochondrial fission-related genes, including *Dnm1l*, *Fis1*, and *Mff*, could modulate energy metabolism in ESCs [48]. Here, we aimed to investigate the effect of knockout of *Dnm1l*, which is the most effective gene for metabolic change in ESCs, on energy metabolism, the cell cycle, stress-related phenotypes, and differentiation ability in ESCs.

Materials and methods

Chemicals

Chemicals were purchased from Sigma Chemical Co. (St. Louis, MO) unless stated otherwise.

CRISPR/cas9 construct design

Clustered regularly interspaced short palindromic repeats (CRISPR)/cas9 single guide RNA (sgRNA) design tool, developed by Dr. Zhang's laboratory (http://zlab.bio/guide-design-resources), was used to design sgRNA for Cas9 nuclease targeting Dnm1l gene in the mouse genome. Target sequences of several genes in exon were selected following the analysis of each gene. The target sequence, 5′-AAGTGT CAGGTTGACAACGT-3′ (20 nucleotides), including the protospacer adjacent motif (PAM; 5′-NGG-3′), was selected for its predicted high score and reduced off-target effects. The sequence including antisense sequence and restriction enzyme site sequence was synthesized as oligomers for cas9/sgRNA expression vector (px330 Cas9/sgRNA dual expression system from Hyongbum Kim's laboratory in Yonsei University (Republic of Korea)) cloning (Bionics, Seoul, Republic of Korea). The process of cloning was as per previous report [44].

Electroporation and establishment of knockout cell line

After E14tg2a mESCs were dissociated into single cells using trypsin–EDTA (Gibco), they (5×10^5 cells/50 µL) were resuspended in R buffer (Neon transfection system, Invitrogen) with 5 µg px330 plasmid vector, which contained dnm1l sgRNA and Cas9. Electroporation was performed with 1200 V, 10 ms width, and 1 pulse, according to the manufacturer's instruction. The electroporated cells were expanded in mESC medium for 3 days. Individual colonies from a single cell were picked and plated onto 96-well plates and expanded. Genomic DNA was extracted using QuickExtract (Epicentre) according to manufacturer's instruction. The target region was amplified, cleaved by T7 endonuclease I (NEB), and subjected to paired-end read sequencing using Illumina MiSeq at LAS (Illumina, San Diego, CA, USA).

Cell culture

E14tg2a (control) and Dnm1l knockout ESCs were cultured on a dish layered with inactivated mouse embryonic fibroblasts (MEFs) in mESC (mouse Embryonic Stem Cell) medium consisting of Dulbecco's modified Eagle's

medium (DMEM) low glucose (Gibco, 11885-084, Gaithersburg, MA, USA) supplemented with 15% heat-inactivated fetal bovine serum (Hyclone; GE Healthcare, Melbourne, VIC, Australia), 1 × penicillin/streptomycin/ glutamine (Gibco), 0.1 mM nonessential amino acids (Gibco), 1 mM β-mercaptoethanol (Gibco), and 10^3 U/mL leukemia inhibitory factor (LIF; ESGRO, Merck Millipore). For three germ layer differentiation, all ESC lines were suspended in a petri dish in the differentiation medium consisting of DMEM low glucose (Hyclone) supplemented with 15% FBS (Hyclone), 1 × P/S/G (Gibco), 0.1 mM NEAA, and 1 mM β-mercaptoethanol (Gibco) for 7 days until the embryoid bodies were formed. Thereafter, the embryoid bodies were attached to the porcine gelatin (Sigma, G9136)-coated dish in DMEM-low medium and cultured for 7 days with a daily change in medium. For differentiation resistance analysis, all the ESC lines were plated on gelatin- or Matrigel-coated dish in N2B27 medium, as described in a previous report [66], supplemented with LIF, with or without 2i inhibitors, namely CHIR99021 (GSKi, 3 μM) and PD0325901 (MEKi, 1 μM).

Immunocytochemistry

Cells were fixed in 4% paraformaldehyde for 20 min at room temperature. After PBS washing, the cells were treated with PBS containing 0.03% Triton X-100 (Sigma) for 5 min and then blocked with PBS containing 3% bovine serum albumin for 1 h at room temperature. Thereafter, cells were probed with primary antibodies against Pou5f1 (Oct4; monoclonal, 1:200, Abcam sc-9081), Nanog (monoclonal, 1:200, Abcam ab80892), tubulin beta III (Tuj1; monoclonal, 1:1000, Millipore MAB1637), smooth muscle actin (SMA; monoclonal, 1:200, Abcam ab7817), and Sox17 (polyclonal, 1:200, R&D systems AF1924). Finally, cells were labeled with secondary antibodies conjugated to Alexa Fluor 488 or 568 (Molecular Probes, Eugene, OR, USA), following specifications of the manufacturer. The mitochondria in live cells were probed with mitoSOX (Invitrogen) following manufacturer's instruction.

RNA isolation and real-time PCR analysis

Total RNA was isolated using a RNeasy Mini Kit (Qiagen, Venlo, Netherlands, http://www.qiagen.com), and then treated with DNase to remove genomic DNA contaminants according to the manufacturer's instructions. cDNA was synthesized from 1 mg total RNA using SuperiorScript III cDNA Synthesis Kit (Enzynomics, Daejeon, Republic of Korea). For real-time PCR, standard curves were created for each target gene primer set using known quantities of total complementary DNA (cDNA), mitochondrial DNA (mtDNA), and nuclear DNA (nDNA) from other cells. PCR reactions were performed in triplicate using a TOPreal™ qPCR 2X PreMIX (Enzynomics, Daejeon, Republic of Korea) and Roche LightCycler 5480 following appropriate instructions. Target genes were amplified by 45 cycles of 95 °C, 60 °C, and 72 °C for 10 s each. We corrected the differences in PCR efficiency between the target and reference loci using efficiency correction in the Relative Quantification Software (Roche LC 480). The primers for real-time PCR are shown in Table 1.

Western blotting

Total cells were lysed using RIPA buffer (Thermo Fisher) according to the manufacturer's instructions. Cell lysates (20 μg protein) were separated on NuPAGE 4–12% Bis–Tris Gels (Invitrogen) and transferred to polyvinyl difluoride membranes. The membranes were blocked using a blocking solution containing 5% skim milk powder and 0.05% Tween 20 in phosphate-buffered saline (PBS). The primary antibodies used in this study were as follows: anti-OCT4 (rabbit, 1:1000; Santa Cruz Biotechnology, Santa Cruz, CA, USA), anti-Nanog (rabbit, 1:1000; Abcam, Cambridge, UK), anti-SOX2 (mouse, 1:1000; Millipore), anti-DRP1 (rabbit, 1:1000; Millipore), and anti-β-actin (mouse, 1:10,000; Sigma). The membranes were incubated with these antibodies overnight at 4 °C. Secondary antibodies were conjugated with anti-mouse IgG-peroxidase (1:10,000; Sigma), anti-goat IgG-horseradish peroxidase (HRP), and anti-rabbit IgG-HRP (1:10,000; Santa Cruz Biotechnology), and the membranes were incubated with these antibodies for 90 min at room temperature. Antigens were detected using Pierce ECL Western Blotting chemiluminescent substrate (Thermo Fisher), according to the manufacturer's instructions. Blots were then exposed to X-ray film for development and stripped for reuse of the membranes. Anti-β-actin antibody (mouse, 1:10,000; Sigma) was used as a control. Densitometry of the protein bands and their loading controls was performed using ImageJ 1.43 (NIH) software. Protein expression levels were normalized to those of Actb.

Teratoma formation

In this study, the cells (5×10^5) were injected into BALB/c nude (5-week-old, male) mice that had been purchased from Orient Bio (Gyeonggi-do, Korea) for experimental purpose. Each cell line was injected into the testis capsule of the mouse. The teratomas formed were harvested from the mouse at 4 weeks post-injection and fixed in 4% paraformaldehyde (Sigma), embedded in paraffin, and sectioned. To analyze the three-germ layer differentiation potential in vivo, the sectioned slides were histologically stained with hematoxylin/eosin (Endoderm), Alcian blue (Mesoderm), and anti-TUJ1 antibody (Ectoderm).

Table 1 Primer sets used for real-time PCR

	Forward	Reverse
Actb	5′-CGCCATGGATGACGATATCG-3′	5′-CGAA GCCGGCTTTGCACAT G-3′
Pou5f1 (Oct4)	5′-GGCTTCAGACTTCGCCTTCT-3′	5′-TGGAAGCTTAGCCAGGTTCG-3′
Nanog	5′-CAGGTGTTTGAGGGTAGCT-3′	5′-CGGTTCATCATGGTACAGTC-3′
Sox2	5′-GCGGAGTGGAAACTTTTGTCC-3′	5′-CGGGAAGCGTGTACTTATCCTT-3′
Keap1	5′-TGCCCCTGTGGTCAAAGTG-3′	5′-GGTTCGGTTACCGTCCTGC-3′
Nfe2l2	5′-TCTTGGAGTAAGTCGAGAAGTGT-3′	5′-GTTGAAACTGAGCGAAAAAGGC-3′
Sod1	5′-AACCAGTTGTGTTGTCAGGAC-3′	5′-CCACCATGTTTCTTAGAGTGAGG-3′
Sod2(mito)	5′-CAGACCTGCCTTACGACTATGG-3′	5′-CTCGGTGGCGTTGAGATTGTT-3′
Sod3	5′-CCTTCTTGTTCTACGGCTTGC-3′	5′-TCGCCTATCTTCTCAACCAGG-3′
Zscan4a	5′-CAGTAGACACCACACAAGAT-3′	5′-GGAAATGAAATGGACTCCTC-3′
Zscan4b	5′-GTAGACACCACACAAGATAG-3′	5′-GACTCCCTTCTTATTACCCA G-3′
Zscan4c	5′-CCGGAGAAAGCAGTGAGGTGGA-3′	5′-CGAAAATGCTAACAGTTGAT-3′
Zscan4d	5′-GTCCTGACAGAGGCCTGCC-3′	5′-GAGATGTCTGAAGAGGCAAT-3′
Zscan4f	5′-CGATATGAGGAGATTCATGGAG-3′	5′-GCTTTTGAAACAACAGCAATC-3′
mtDNA	5′-CTAGCAGAAACAAACCGGGC-3′	5′-CCGGCTGCGTATTCTACGTT-3′
nDNA	5′-CCGCAAGGGAAAGATGAAAGAC-3′	5′-TCGTTTGGTTTCGGGGTTTC-3′
telomere	5′-CGGTTTGTTTGGGTTTGGGTTTGGG TT TGGGTTTGGGTT-3′	5′-GGCTTGCCTTACCCTTACCCTTAC CCTTACCCTTACCCT-3′
36B4	5′-ACTGGTCTAGGACCCGAGAAG-3′	5′-TCAATGGTGCCTCTGGAGATT-3′

Electron microscopy

For transmission electron microscopy (TEM), samples were fixed in 4% paraformaldehyde (Sigma) and 2.5% glutaraldehyde (Sigma) in a 0.1 M phosphate (Sigma) buffer for 24 h. After washing with 0.1 M phosphate buffer, the samples were post-fixed in 1% osmium tetroxide (Sigma) containing 0.1 M phosphate buffer for 1 h. Next, the samples were serially dehydrated with graded ethanol (Merck Millipore). The dehydrated samples were embedded in Epon 812 and incubated at 60 °C for 3 days for polymerization. Ultrathin Sections (60–70 nm) were obtained by ultramicrotome (Leica Ultracut UCT). Ultrathin sections collected on a grid (200 mesh) were examined by a TEM (JEM 1010) operating at 60 kV, and images therefrom were recorded by a charge-coupled device (CCD) camera (SC1000; Gatan).

Mitochondrial length analysis

Images from electron microscopy were analyzed and measured using the ImageJ 1.43 (NIH) software for calculating the maximum (Max)/minimum (Min) ratio of mitochondrial length. At least over fifty mitochondria were measured and analyzed per sample to obtain reliable data.

Flow cytometry analysis

Each cell line was enzymatically dissociated by 0.25% trypsin with mechanical pipetting and washed twice by phosphate-buffered saline (PBS, Welgene, Gyeongsan, Korea). After centrifugation at 1500 rpm for 5 min and removal of supernatant, 70% ethanol was added slowly dropwise while vortexing moderately. The fixed cells were stored at 4 °C for 2 h. After centrifugation at 2000 rpm for 7 min and removal of ethanol, the fixed cells were washed twice with PBS. Thereafter, the fixed cells were resuspended in propidium iodide staining solution (50 µg/mL of propidium iodide (PI; Sigma) and 2 µg/mL of DNase-free RNase (Thermo Fisher Scientific)) and incubated for 10 min at 37 °C in the dark. Stained cells were filtered through a 70-µm nylon mesh (Falcon) to remove any cell clump. Flow cytometry was performed using a CytoFLEX Flow Cytometer (Beckman Coulter) following the manufacturer's instructions.

Oxygen consumption rate analysis

For measuring the oxygen consumption rate (OCR), we used the Seahorse extracellular flux (XFp) analyzer. A total 2×10^4 cells of the control or Dnm1l knockout ESC were attached in XFp Cell Culture Microplate pre-coated with FBS in mESC medium 24 h before the assay. After the medium change to XF base media supplemented with D-glucose (1 g/L), Sodium pyruvate (1 mM) and L-glutamine (4 mM), the assay was performed by using XFp Extracellular Flux Analyzer (Seahorse Bioscience, North Billerica, MA, USA). Five measurements were obtained under basal conditions and after the addition of several chemicals such as oligomycin (1 µM), FCCP (2 µM) and rotenone (1 µM)/antimycin A (1 µM). The process after treatment was performed following the manufacturer's instructions.

Extracellular acidification analysis

To measure the extracellular acidification rate (ECAR), we used a Seahorse extracellular flux (XF96) analyzer. A total of 1.5×10^4 cells were cultured in XF96 Cell Culture Microplate, pre-coated with Matrigel in mESC medium, 24 h before the assay. After a medium change to XF base media supplemented with L-glutamine (4 mM, Gibco, 25030-081), the assay was performed using XF96 Extracellular Flux Analyzer (Seahorse Bioscience, North Billerica, MA, USA). Four measurements were obtained under basal conditions and after the addition of several chemicals, such as D-glucose (10 mM), oligomycin (1 μM), and 2-deoxy-D-glucose (50 mM) (Agilent Technologies, 103020-100). The process after treatment was performed according to the manufacturer's instructions.

Direct measurement of adenosine triphosphate level

To measure the adenosine triphosphate (ATP) levels, we used a luminescent ATP detection assay kit (Abcam, ab113849) with GloMax 96 Microplate Luminometer (Promega, E6521, Madison, WI, USA). A total of 1×10^4 cells were cultured in 96-well cell culture plates (SPL life science, 30296, Gyeonggi-do, Korea) pre-coated with Matrigel in mESC medium, 24 h prior to the assay. The process after treatment was performed according to the manufacturer's instructions.

Direct measurement of the alpha-ketoglutarate amount

To measure the amount of alpha-ketoglutarate, we used a colorimetric alpha-ketoglutarate assay kit (Sigma, MAK054) with xMark Microplate Absorbance Spectrophotometer (Bio-RAD, 1681150, Hercules, CA, USA). A total of 1×10^4 cells were cultured in 96-well cell culture plates (SPL life science, 30196, Gyeonggi-do, Korea), pre-coated with Matrigel in mESC medium, 24 h prior to the assay. The process after treatment was performed according to the manufacturer's instructions.

Detection of reactive oxygen species

To detect reactive oxygen species, we used the cell-permeant reagent 2', 7' -dichlorofluorescein diacetate (DCF-DA) in the cellular ROS assay kit (Abcam, ab113851). A total of 1×10^4 cells were cultured in 96-well cell culture plates (SPL life science, 30196, Gyeonggi-do, Korea), pre-coated with Matrigel in mESC medium, 24 h prior to the assay. The process after treatment was performed according to the manufacturer's instructions.

RNA-seq analysis

Total RNA samples were converted into cDNA libraries using the TruSeq Stranded mRNA Sample Prep Kit (Illumina). Starting with 100 ng of total RNA, polyadenylated RNA (mainly mRNA) was selected and purified using oligo dT-conjugated magnetic beads. This mRNA was physically fragmented and converted into single-stranded cDNA using reverse transcriptase and random hexamer primers, with the addition of Actinomycin D to suppress DNA-dependent synthesis of the second strand. Double-stranded cDNA was created by removing the RNA template and synthesizing the second strand in the presence of dUTP (deoxy-ribo-uridine triphosphate) in place of dTTP (deoxythymidine triphosphate). A single A base was added to the 3 prime end to facilitate ligation of sequencing adapters, which contain a single T base overhang. Adapter-ligated cDNA was amplified by polymerase chain reaction to increase the amount of sequence-ready library. During this amplification, the polymerase stalls when it encounters a U base, rendering the second strand a poor template. Accordingly, the amplified material used the first strand as a template, thereby preserving the strand information. Final cDNA libraries were analyzed for size distribution and using an Agilent Bioanalyzer (DNA 1000 kit; Agilent), quantitated by qPCR (Kapa Library Quant Kit; Kapa Biosystems, Wilmington, MA, USA), then normalized to 2 nM in preparation for sequencing.

Validity of sequenced reads were accessed with FastQC (v0.11.5) and the reads were aligned with STAR (v2.5.2b) to UCSC mouse mm10 genome assembly. StringTie (v1.3.3b) was used to process STAR results into transcript assemblies. Results from StringTie were used to calculate average expression of each gene in FPKM and the acquired values were used for drawing scatter plots in R (v3.6.1). Read counts were normalized for read depth and analyzed using the BioJupies package [54] with default parameters. A notebook containing the code, a list of differentially expressed genes and an overview of the analysis can be found at the following URL: https://amp.pharm.mssm.edu/biojupies/notebook/CKbmUQhlJ.

Ethics statement for animal use

Experiments were performed following the approved guidelines and all experimental protocols were approved by the Institutional Animal Care and Use Committee (IACUC) of Konkuk University. All mouse strains were bred and housed at the mouse facility of the Konkuk University or were purchased from Orient-Bio Inc. (Gyeonggi-do, Korea; http://www.orient.co.kr). Animal welfare was under the control of local committees. Mice were housed in a temperature-controlled room with automated darkness-light cycle system and fed with a regular ad libitum feeding. Before testis

harvesting, the mice were sacrificed by carbon dioxide inhalation.

Statistical analysis

All experiments were performed in triplicate and data represented as means ± standard deviation. The significance of differences was assessed by an unpaired two-tailed student's t test, one-way analysis of variance (ANOVA) with Tukey's Honestly Significant Difference post hoc for multiple comparisons. p values < 0.05 were considered statistically significant.

Results

Characterization of the pluripotency of *Dnm1l*$^{-/-}$ embryonic stem cells (ESCs)

We previously reported that knockout of mitochondrial fission genes, *Dnm1l*, could maintain pluripotency; however, loss of this gene induced metabolic changes in ESCs [48]. *Dnm1l* biallelic knockout (at Exon 5) mouse ESCs were generated by the CRISPR/cas9 gene-editing system (Fig. S1A). Since monoallelic *Dnm1l*$^{\pm}$ ESCs showed a negligible difference in several aspects compared with wild-type ESCs (data not shown), biallelic *Dnm1l*$^{-/-}$ ESCs were used for further analyses. Thereafter, we assessed whether any off-target mutations occurred in biallelic *Dnm1l*$^{-/-}$ ESCs. Whole genome sequencing analysis revealed that there was an indel on-target site (Fig. S1B). However, there were no possible indels in various predicted off-target sites (Fig. S1C).

Dnm1l$^{-/-}$ ESCs self-renewed with normal morphology of dome-like colonies and stained positive for major pluripotency markers, Oct4 and Nanog (Fig. 1A, B). Thereafter, the transcript and protein levels of core pluripotency markers, such as *Oct4*, *Sox2*, and *Nanog*, were assessed in *Dnm1l*$^{-/-}$ ESCs (Fig. 1C, D). Notably, *Dnm1l*$^{-/-}$ ESCs showed marginally lower levels of *Oct4*, similar levels of *Sox2*, and almost twice the levels of *Nanog* transcripts (Fig. 1C). This result was confirmed at the protein level using western blotting (Fig. 1D). Both Oct4 protein and mRNA levels decreased marginally in *Dnm1l*$^{-/-}$ ESCs (Fig. 1C, D). Sox2 protein levels decreased in *Dnm1l*$^{-/-}$ ESCs despite the similar mRNA levels to those of control ESCs (Fig. 1C, D). Notably, the protein as well as mRNA levels of Nanog increased in *Dnm1l*$^{-/-}$ ESCs (Fig. 1C, D). In line with core triad pluripotent gene expression [33], other pluripotency genes were also differentially expressed in *Dnm1l*$^{-/-}$ ESCs compared with those in control ESCs (Fig. S2A).

To test the differentiation potential of all three germ layers [6], the teratoma formation assay and in vitro differentiation analysis were conducted using *Dnm1l*$^{-/-}$ and control ESCs. The *Dnm1l*$^{-/-}$ ESCs differentiated into all three germ layers, including smooth muscle actin (SMA, mesoderm), endothelium (Sox17, endoderm), and neuron (Tuj1, ectoderm), in vitro (Fig. S2B). The teratoma formation assay revealed that *Dnm1l*$^{-/-}$ ESCs could form teratomas (Fig. 1E) containing endodermal (gut epithelium), mesodermal (cartilage), and ectodermal (Tuj1^{+} neuron) tissues (Fig. 1F). The size of teratoma formed from *Dnm1l*$^{-/-}$ ESCs was significantly smaller than that of teratoma formed from control ESCs (Fig. 1E). Collectively, these findings indicated that knockout of *Dnm1l* in ESCs could affect the expression pattern of pluripotency genes, but the ability of ESCs to self-renew and differentiate potential to the three germ layers was not severely affected.

Intracellular characteristics of *Dnm1l*$^{-/-}$ ESCs

As *Dnm1l* is one of the mitochondrial fission-related genes, changes in the mitochondrial morphology of *Dnm1l*$^{-/-}$ ESCs were examined using electron microscopy (Fig. 1G). As expected, the morphology of the mitochondria of *Dnm1l*$^{-/-}$ ESCs was distinct from that of control ESCs (Fig. 1G). Generally, the morphology of mitochondria in ESCs and other pluripotent stem cell types is globular-shaped with immature cristae [8, 13, 14]. The mitochondria of *Dnm1l*$^{-/-}$ ESCs were more elongated and rod-shaped and showed more mature cristae than those of the control ESCs (Fig. 1G, left). Next, we measured the calculated-maximal (c-max) and calculated-minimal (c-min) lengths of mitochondria in the control and *Dnm1l*$^{-/-}$ ESCs (Fig. 1G, right). The ratio values of c-max/c-min from control ESCs (1.41) and *Dnm1l*$^{-/-}$ ESCs (2.06) indicated that the mitochondria of *Dnm1l*$^{-/-}$ ESCs were more elongated than those of control ESCs (Fig. 1G).

Dnm1l deletion in ESCs results in metabolic changes and excessive reactive oxygen species (ROS) production

We performed a series of analyses to clarify how the deletion of *Dnm1l* alters the cellular metabolic processes in ESCs. Considering the coupling of mitochondrial fission and mitochondrial metabolic pathways such as glycolysis, tricarboxylic acid cycle, and oxidative phosphorylation [18], we hypothesized that *Dnm1l* deficiency might influence overall cellular metabolism. As previously reported [48], *Dnm1l*$^{-/-}$ ESCs are more dependent on the OXPHOS than on glycolysis (Fig. 2A, B). Likewise, XF cell energy phenotype analysis showed that *Dnm1l*$^{-/-}$ ESCs moved to the energetic phase, indicating that *Dnm1l*$^{-/-}$ ESCs utilized OXPHOS upon oxidative stress or excessive energy demand, whereas control ESCs moved to the glycolytic phase (metabolic state focused on producing cellular compounds). These

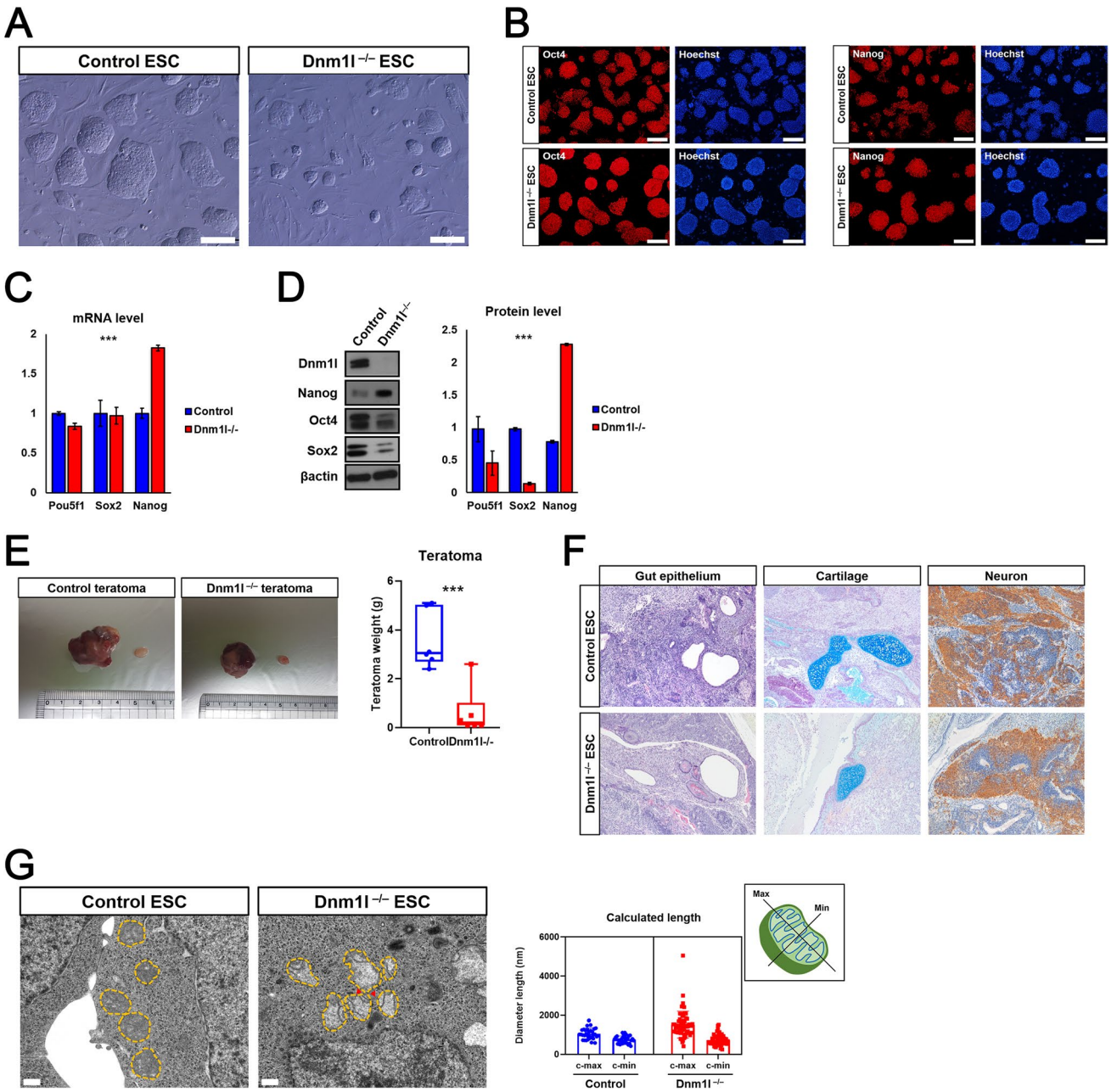

Fig. 1 Generation and characterization of *Dnm1l*$^{-/-}$ embryonic stem cells (ESCs). **A** Bright field images of control and *Dnm1l*$^{-/-}$ ESCs. **B** Immunocytochemical analysis of the pluripotency markers, NANOG (top) and OCT4 (bottom) in control and *Dnm1l*$^{-/-}$ embryonic stem cells (ESCs). Scale bars: 200 µm. **C** Real time-polymerase chain reaction (PCR) analysis of core pluripotent genes, including *Pou5f1* (*Oct4*), *Sox2*, and *Nanog*, in control and *Dnm1l*$^{-/-}$ ESCs. Data are presented as the mean ± SEM of the values from three independent experiments. **D** Western blot analysis of core pluripotent and Dnm1l proteins in control and *Dnm1l*$^{-/-}$ ESCs. Data are presented as the mean ± SEM of values from three independent experiments. **E**, **F** Teratoma formation and analysis of in vivo differentiation potential. **E** Teratoma formation in control and *Dnm1l*$^{-/-}$ ESCs. Control ESC-derived teratomas were larger than *Dnm1l*$^{-/-}$ ESC-derived teratomas. An unpaired t test: ***$p < 0.001$. **F** Control and *Dnm1l*$^{-/-}$ ESC-derived teratomas were histologically stained with hematoxylin/eosin (Gut epithelium, Endoderm, arrowed), alcian blue (Cartilage, Mesoderm, arrowed), anti-tuj1 antibody (Neuron, Ectoderm), which represents the in vivo differentiation potential of three germ layers. **G** Enlarged TEM images of control and *Dnm1l*$^{-/-}$ ESC lines focused on the mitochondria (yellow dot lines). Most mitochondria in *Dnml1*$^{-/-}$ ESCs were elongated owing to fission failure (red arrows). Scale bars: 0.5 µm. Calculated length of mitochondrial max/min values, using the ImageJ software, in control and *Dnm1l*$^{-/-}$ ESC lines. Criteria used for analyzing mitochondrial maximal (Max) or minimal (Min) length of all ESC lines

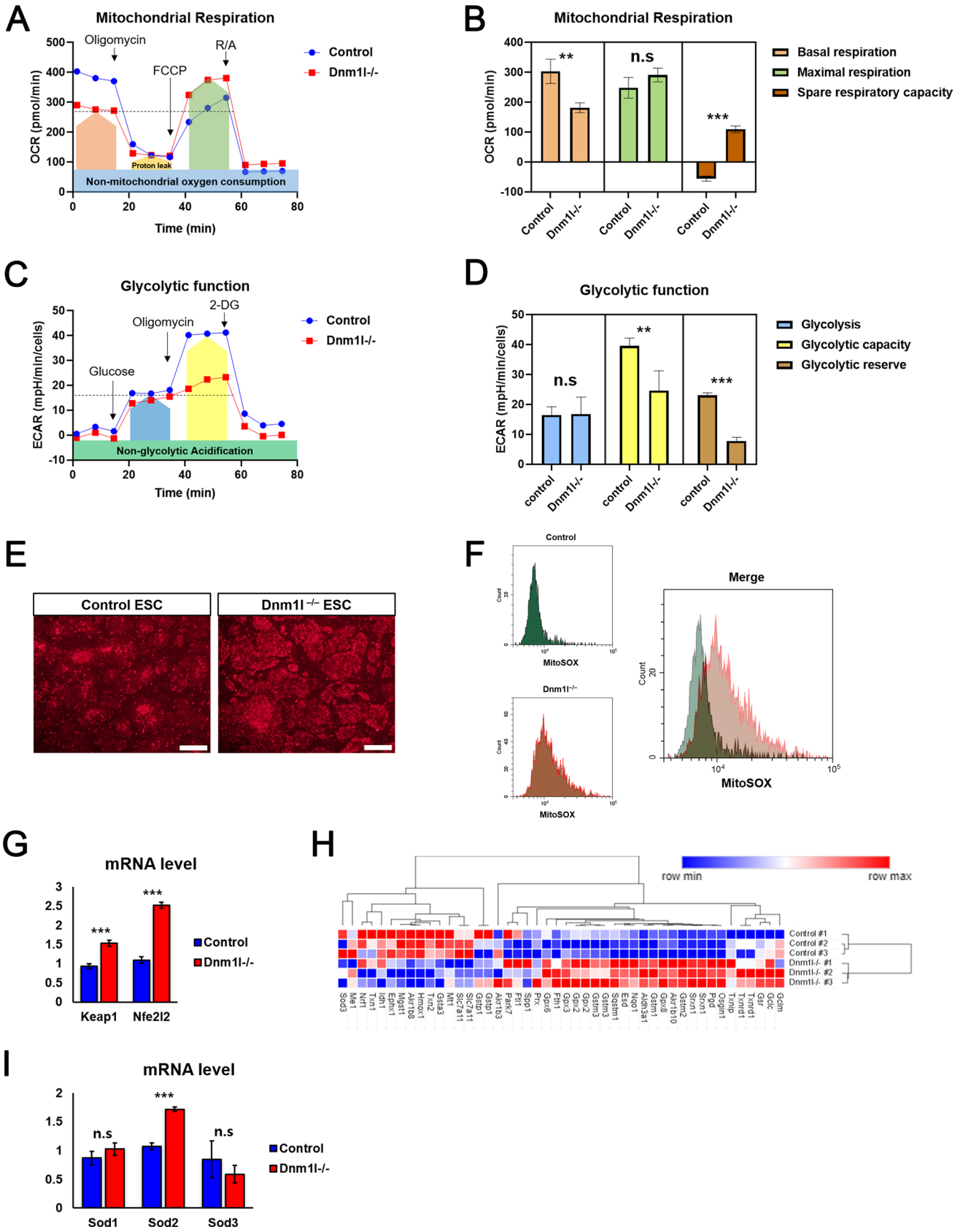
A
Mitochondrial Respiration
Oligomycin
FCCP
R/A
Proton leak
Non-mitochondrial oxygen consumption
OCR (pmol/min)
Time (min)
Control
Dnm1l-/-
B
Mitochondrial Respiration
**
n.s
***
OCR (pmol/min)
Basal respiration
Maximal respiration
Spare respiratory capacity
C
Glycolytic function
2-DG
Oligomycin
Glucose
Non-glycolytic Acidification
ECAR (mpH/min/cells)
Time (min)
D
Glycolytic function
n.s
**
***
ECAR (mpH/min/cells)
Glycolysis
Glycolytic capacity
Glycolytic reserve
E
Control ESC
Dnm1l −/− ESC
F
Control
MitoSOX
Dnm1l-/-
Merge
Count
G
mRNA level
***
Keap1
Nfe2l2
H
row min
row max
Control #1
Control #2
Control #3
Dnm1l-/- #1
Dnm1l-/- #2
Dnm1l-/- #3
I
mRNA level
n.s
***
Sod1
Sod2
Sod3

◂**Fig. 2** Metabolic analysis of control and *Dnm1l*$^{-/-}$ embryonic stem cells (ESCs). **A** Measurement of oxygen consumption rate (OCR) in control and *Dnm1l*$^{-/-}$ ESCs. **B** Measurement of basal respiration, maximal respiration, spare respiratory capacity in control and *Dnm1l*$^{-/-}$ ESCs. Oligomycin; an ATP synthase inhibitor, *p*-trifluoromethoxyphenylhydrazone (FCCP); an uncoupling agent that collapses the proton gradient, R/A (rotenone/antimycin); a complex I inhibitor/a complex III inhibitor. **C** Measurement of extracellular acidification rate (ECAR) in control and *Dnm1l*$^{-/-}$ ESCs. **D** Measurement of glycolysis, glycolytic capacity, glycolytic reserve in control and *Dnm1l*$^{-/-}$ ESCs. 2-DG (2-deoxy-glucose); a glucose analog, inhibiting glycolysis through competitive binding to glucose hexokinase. **E** Representative image of control and *Dnm1l*$^{-/-}$ ESC lines observed using mitoSOX. **F** Flow cytometry analysis of the proportion of control and *Dnm1l*$^{-/-}$ ESCs stained with mitoSOX. **G** Real time-polymerase chain reaction (PCR) analysis of ROS-related genes, including *Keap1* and *Nfe2l2* (Nrf2), in control and *Dnm1l*$^{-/-}$ ESCs. An unpaired t test: $***p < 0.001$. Data are presented as the mean ± SEM of values from three independent experiments. **H** Heatmap of Nrf2 target gene expression patterns in control and *Dnm1l*$^{-/-}$ ESCs. **I** Real time-PCR analysis of superoxide dismutase 1, 2 (mitochondria-specific), and 3 in control and *Dnm1l*$^{-/-}$ ESCs. An unpaired t test: $***p < 0.001$, *n.s* not significant. Data are presented as the mean ± SEM of values from three independent experiments

results indicate that knockout of *Dnm1l* in ESCs triggers a metabolic shift from glycolysis to OXPHOS (Fig. S3A). In particular, *Dnm1l*$^{-/-}$ ESCs displayed higher spare respiratory capacity (SRC) and lower glycolytic capacity than control ESCs (Fig. 2B and D). Also, *Dnm1l*$^{-/-}$ ESCs displayed lower proton leak than control ESCs (Fig. S3B). Thereafter, total cellular ATP concentration was determined using the luminescent ATP detection assay (Fig. S3C). As expected, (from the higher SRC levels), *Dnm1l*$^{-/-}$ ESCs produced more intracellular ATP than the control ESCs (Fig. 2B, Fig. S3C). Besides, *Dnm1l*$^{-/-}$ ESCs displayed higher non-mitochondrial oxygen consumption (Fig. S3D).

As *Dnm1l*$^{-/-}$ ESCs used more aerobic metabolism than control ESCs, we hypothesized that the mitochondria of *Dnm1l*$^{-/-}$ ESCs may produce more ROS. To this end, superoxide levels were measured using MitoSOX™ Red, which exhibits red fluorescence when oxidized by superoxide radicals [24]; the more superoxide levels, the more red fluorescence is emitted (Fig. 2E). As expected, the mitochondria of *Dnm1l*$^{-/-}$ ESCs produced more superoxide than the control ESCs (Fig. 2E). Thereafter, fluorescence-activated cell sorting (FACS) analysis also confirmed increased MitoSOX-reactive fluorescence in *Dnm1l*$^{-/-}$ ESCs than in control ESCs (Fig. 2F).

Next, we analyzed the expression patterns of ROS-related genes. Nrf2 regulates the gene expression of endogenous antioxidant synthesis and ROS-eliminating proteins [23]. To this end, genes related to the glutathione metabolic process, such as *Keap1* and *Nfe2l2* (*Nrf2*), were overexpressed in *Dnm1l*$^{-/-}$ ESCs (Fig. 2G). To gain a better understanding of the Nrf2 signaling cascade, expression patterns of Nrf2 target genes that were reported previously [31, 39, 53] were investigated (Fig. 2H). Forty Nrf2 target genes were found to be differentially expressed between the *Dnm1l*$^{-/-}$ and control ESCs. Notably, mitochondrial superoxide dismutase 2 (*Sod2*) was overexpressed in *Dnm1l*$^{-/-}$ ESCs, while the expression levels of *Sod1* and *Sod3* were similar (Fig. 2I). Collectively, these results demonstrated that *Dnm1l* deficiency in ESCs caused an increase in OXPHOS, which is closely related to excessive ROS production and subsequently triggers the Nrf2 signaling cascade.

Dnm1l deletion in ESCs induces telomere shortening and the activation of 2-cell-stage-specific genes

Several studies have reported that loss of *Dnm1l* results in cell cycle perturbation in *Drosophila melanogaster* [32], breast cancer cells [43], and normal rat kidney cells [34]. To broaden the knowledge of the effect of *Dnm1l* deficiency in the cell cycle of pluripotent stem cells, the cell cycle was investigated in *Dnm1l*$^{-/-}$ ESCs. *Dnm1l*$^{-/-}$ ESCs formed a smaller colony than the control ESCs after 3 days of passaging (Fig. 3A). In addition, the proliferation assay revealed that the proliferation rate of *Dnm1l*$^{-/-}$ ESCs was much lower than that of control ESCs (Fig. 3B). As cell cycles were extended in response to telomere shortening to repair telomeres [38], telomere lengths in the control and *Dnm1l*$^{-/-}$ ESCs were compared. Telomere length in *Dnm1l*$^{-/-}$ ESCs was found to be shorter than that in control ESCs (Fig. 3C). Thereafter, we further analyzed detailed cell cycle phases of *Dnm1l*$^{-/-}$ ESCs using FACS analysis after propidium iodide staining. Normal ESCs are known to display extremely rapid and distinct cell division cycles compared with other somatic cell types [62]. The cell cycle of *Dnm1l*$^{-/-}$ ESCs was compared with that of control ESCs and fibroblast cells as experimental controls (Fig. 3D). Fibroblasts primarily remained in the G0/G1 phase (80.08%), while control ESCs showed a much lower ratio of the G0/G1 phase (43.39%) and much higher ratios of the S (34.51%) and G2/M phases (22.34%) (Fig. 3D, left and middle), confirming the rapid and distinct cell division cycle of pluripotent ESCs. Although the S phase ratio of *Dnm1l*$^{-/-}$ ESCs (33.26%) was indistinguishable from that of control ESCs (34.51%), the G2/M phase ratio of *Dnm1l*$^{-/-}$ ESCs (32.88%) was much higher than that of control ESCs (22.34%) (Fig. 3D, middle and right). The ratios of the G0/G1 phase of *Dnm1l*$^{-/-}$ ESCs (33.65%) were much lower than those of control ESCs (43.39%) (Fig. 3D, middle and right). Considering the slower proliferation of *Dnm1l*$^{-/-}$ ESCs than the controls, *Dnm1l* deficiency in ESCs may be affected by cell cycle length of the G0/G1 and G2/M phase.

Telomere repair and elongation systems are activated upon telomere shortening, and telomeres could be effectors in cell cycle change [19, 37, 38, 64, 67, 69]. Thus, we subsequently analyzed the expression levels of telomere

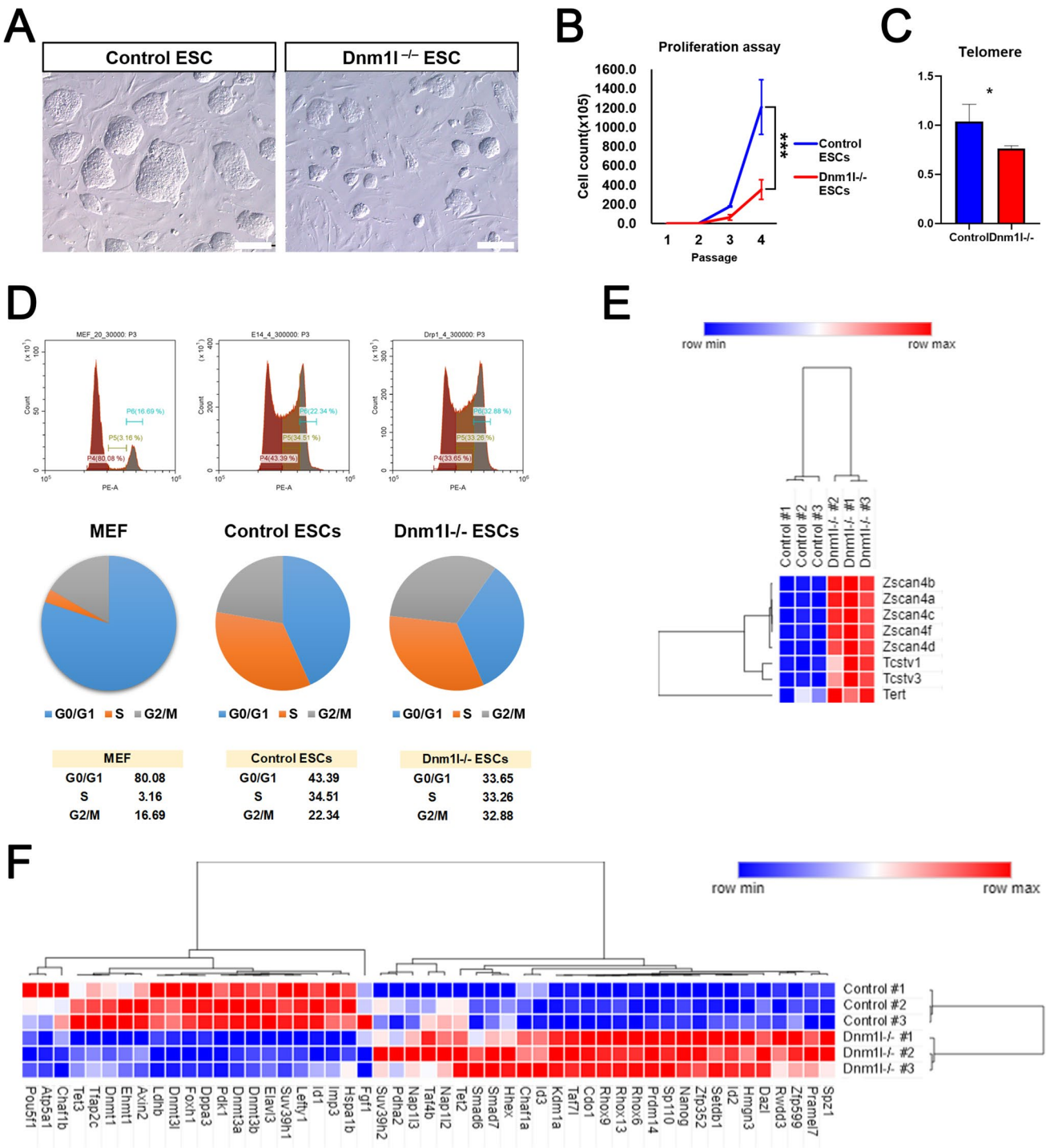

Fig. 3 Cell cycle analysis of control and *Dnm1l*$^{-/-}$ embryonic stem cells (ESCs). **A** Representative image of control and *Dnm1l*$^{-/-}$ ESC lines observed after 3 days of cell expansion. Scale bars: 200 µm. **B** Proliferation assay of control and *Dnm1l*$^{-/-}$ ESCs. An unpaired t test: ***$p < 0.001$. Data are presented as the mean ± SEM of values from three independent experiments. **C** Relative quantification of telomere length was performed on control and *Dnm1l*$^{-/-}$ ESC samples in triplicate using real time-polymerase chain reaction (PCR) via amplification of telomeres relative to the amount of nDNA. An unpaired t test: *$p < 0.05$. Data are presented as the mean ± SEM of values from three independent experiments. **D** Flow cytometry analysis of the proportion of control and *Dnm1l*$^{-/-}$ ESCs, and fibroblasts (control) stained with propidium iodide (PI; top), and their pie charts (middle). Ratio information of each pie chart (bottom). **E** Heatmap of expression patterns of genes related to telomere elongation in control and *Dnm1l*$^{-/-}$ ESCs. **F** Heatmap of 2-cell-like cell genes expression patterns in control and *Dnm1l*$^{-/-}$ ESCs

elongation-related genes, such as *Zscan4*, *Tcstv1/3*, and *Tert,* in *Dnm1l*$^{-/-}$ ESCs. As expected, the *Zscan4* family, *Tcstv1/3*, and *Tert* genes were overexpressed in *Dnm1l*$^{-/-}$ ESCs (Fig. 3E). *Zscan4* becomes active after sensing shortened telomeres, which extends the cell cycle length owing to the repair of the telomere presumably at the G2/M phase [38]. The Zscan4 protein is known to directly elongate the telomere via homologous recombination following the recruitment of SPO11 [67]. In addition, ectopic expression of *Tcstv1/3* extends telomere length in ESCs with Zscan4 activation [69]. As *Zscan4* is a marker for the 2-cell-stage embryo [46], we further analyzed the expression levels of other 2-cell-stage-specific genes. Diego et al. reported that a small number of cells expressing 2-cell-stage-specific genes are present among cultured ESCs [46]. Notably, most 2-cell-stage-specific genes were found to be differentially expressed in *Dnm1l*$^{-/-}$ ESCs (Fig. 3F). Collectively, these data suggest that deletion of *Dnm1l* in ESCs results in a change in the expression levels of 2-cell-stage-specific genes and reduced proliferation rates, which may be induced by G2/M retardation and telomere shortening.

Dnm1l deletion in ESCs attenuates the dissolution of pluripotency under differentiation induction

As mentioned above, *Dnm1l*$^{-/-}$ ESCs have distinct cell cycle and differential expression of 2-cell-stage-specific genes. Previous studies reported that ESCs have an increased susceptibility to differentiation during the G1 phase [9, 42]. Thus, we hypothesized that the lower ratio of the G0/G1 phase in *Dnm1l*$^{-/-}$ ESCs might attenuate the dissolution of pluripotency or hamper the differentiation from the pluripotent state (Fig. 3D, right). To confirm this, the *Dnm1l*$^{-/-}$ and control ESCs were differentiated for 14 days via embryoid body (EB) formation in vitro. Notably, most *Dnm1l*$^{-/-}$ ESCs maintained Oct4 expression, while Oct4-expressing cells were not examined in differentiation-induced cells from control ESCs (Fig. 4A), indicating the suppressive effect of *Dnm1l* deficiency on differentiation. Moreover, *Dnm1l*$^{-/-}$ ESCs maintained high levels of *Nanog*; however, control ESCs did not express *Nanog* after 14 days of differentiation (Fig. 4B). When these differentiated cells from *Dnm1l*$^{-/-}$ ESCs were replated on ESC culture medium (+LIF), AP-positive ESC colonies were formed (Fig. 4C), confirming that several *Dnm1l*$^{-/-}$ ESCs maintained a pluripotent state even after 14 days of differentiation induction.

Recently, Santosha et al. demonstrated that α-ketoglutarate is related to Nanog expression and enhances the self-renewal ability of ESCs [55]. Thus, the amount of α-ketoglutarate was measured in *Dnm1l*$^{-/-}$ ESCs. As expected, *Dnm1l*$^{-/-}$ ESCs contained a higher amount of α-ketoglutarate than control ESCs (Fig. 4D), indicating the correlation between *Nanog* upregulation and the level of α-ketoglutarate in *Dnm1l*$^{-/-}$ ESCs. Thereafter, we investigated whether the gene expression levels of *Nanog* could affect the dissolution of pluripotency in *Dnm1l*$^{-/-}$ ESCs. To induce the upregulation of Nanog, we treated *Dnm1l*$^{-/-}$ and control ESCs with two small molecule inhibitors (2i), PD032591 (MEK inhibitor) and CHIR99021 (GSK3 inhibitor), which are known to positively regulate Nanog [33]. PSCs cultured in a medium containing 2i without a feeder layer were maintained in a naïve pluripotent state [2]. Thus, we tested whether *Dnm1l*$^{-/-}$ ESCs, which expressed high Nanog levels, could self-renew without 2i. Control ESCs self-renewed and formed colonies in naïve pluripotency medium in the presence of 2i; however, they could not maintain ESC colonies in the absence of 2i (Fig. 4E, F). Surprisingly, *Dnm1l*$^{-/-}$ ESCs retained colonies over five passages in the naïve pluripotency medium even without 2i (Fig. 4E, F), indicating that higher levels of Nanog in *Dnm1l*$^{-/-}$ ESCs could compensate the effects of MEK and GSK3 inhibition induced by 2i treatment (Fig. 4E, F). These results suggest that upregulated *Nanog* expression may be the cause of the attenuation of pluripotency dissolution in *Dnm1l*$^{-/-}$ ESCs.

G2/M stage retardation in ESCs causes attenuation of the dissolution of pluripotency

Thereafter, we determined whether G2/M stage retardation could be an effector for the inhibition of differentiation of ESCs. Accordingly, we tested whether cell cycle retardation in the G2/M phase, which is a phenotype of *Dnm1l* deletion, leads to the inhibition of differentiation in wild-type ESCs. Charles et al. reported that RO-3306, an ATP-competitive and selective CDK1 inhibitor, and ABT-75, a microtubule polymerization inhibitor, are reversible cell cycle arrest inducers that can be used for cell cycle synchronization via the G2/M block [65]. Excessive concentration of these inhibitors caused cell cycle arrest and ESCs remained in a single cell state without colony formation (Fig. S4A). Thus, to induce cell cycle retardation, which may induce the formation of smaller colonies, wild-type ESCs were treated with permissive concentrations of RO-3306 and ABT-75 in ESC medium (Fig. 5A). ABT-751 treatment (100 and 300 nM) for 3 days could induce cell cycle retardation (forming smaller colonies); however, it did not affect the expression levels of *Nanog* (Fig. 5B). RO-3306 treatment at higher concentrations of 3 and 5 μM induced cell cycle retardation with upregulation of *Nanog*, approximately 2- and 3.5-fold, respectively (Fig. 5A and B). Collectively, treatment with 3 μM RO-3306 simulated the effect of *Dnm1l* deletion, i.e., G2/M phase retardation and twofold expression of *Nanog*. Thereafter, we investigated whether RO-3306 treatment (3 μM) could affect the differentiation potential of ESCs. Notably, 3 μM RO-3306-treated ESCs showed a tendency to not differentiate;

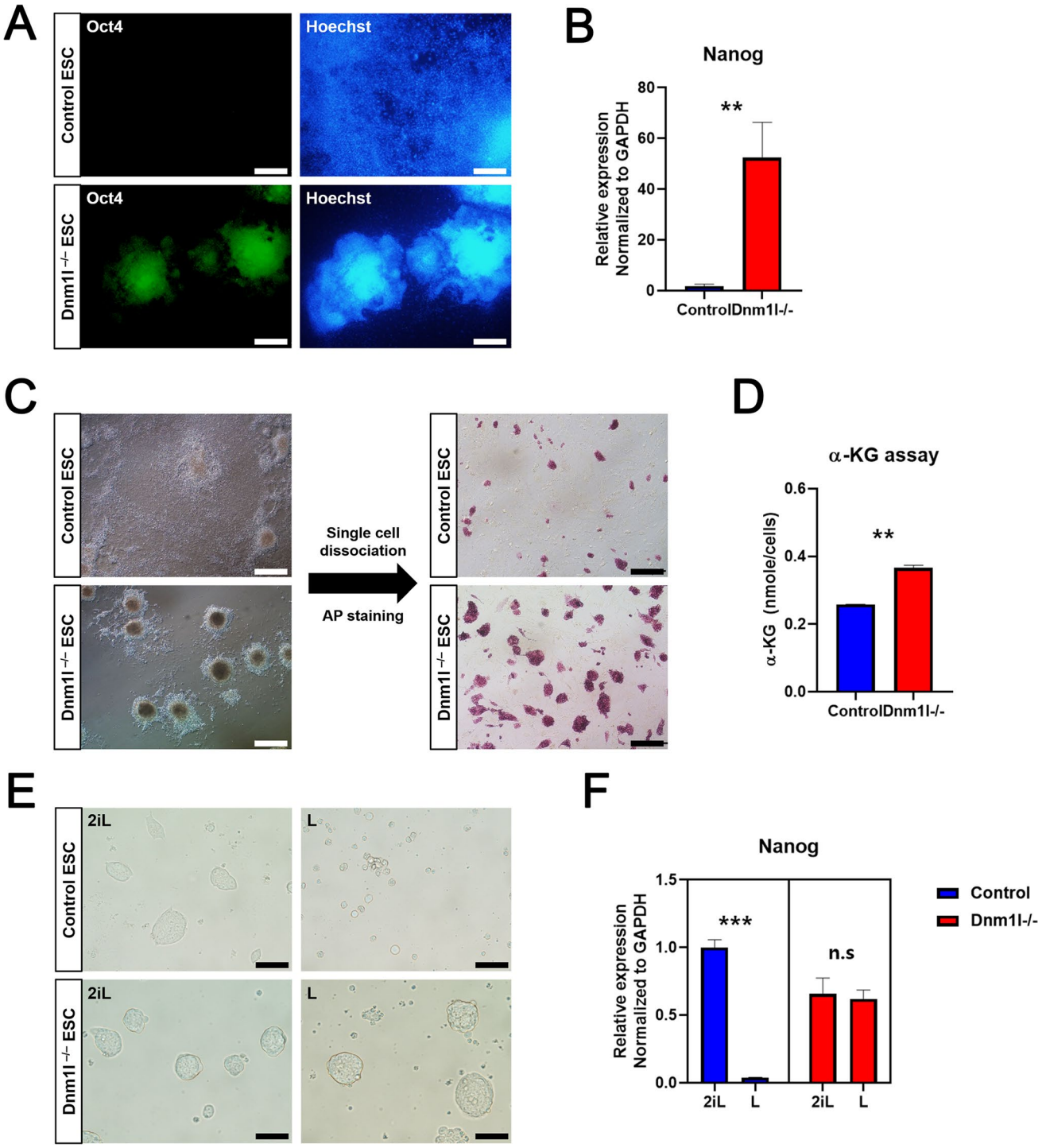

Fig. 4 *Dnm1l* deficiency in mouse embryonic stem cells (ESCs) decreases the population of differentiated cells under stimulation of exit from pluripotency. **A** Immunocytochemical analysis of the Oct4 protein in control and *Dnm1l*$^{-/-}$ ESCs after 14 days of spontaneous differentiation. Scale bars: 200 µm. **B** Real time-polymerase chain reaction (PCR) analysis of *Nanog* in control and *Dnm1l*$^{-/-}$ ESCs at day 14 of spontaneous differentiation. An unpaired t test: $^{**}p < 0.01$. Data are presented as the mean ± SEM of values from three independent experiments. **C** Representative image of control and *Dnm1l*$^{-/-}$ ESC lines observed after 14 days of spontaneous differentiation (left) and alkaline phosphatase staining (right). Scale bars: 500 µm. **D** The amount of alpha-ketoglutarate in control and *Dnm1l*$^{-/-}$ ESCs. An unpaired t test: $^{**}p < 0.01$. Data are presented as the mean ± SEM of values from three independent experiments. **E** Representative image of control and *Dnm1l*$^{-/-}$ ESC lines observed after 3 days of cell expansion on a gelatin-coated dish in 2iL and L conditions. Scale bars: 100 µm. **F** Real time-PCR analysis of *Nanog* in control and *Dnm1l*$^{-/-}$ ESCs at day 3 of 2iL and L condition culture. An unpaired t test: $^{***}p < 0.001$, *n.s* not significant. Data are presented as the mean ± SEM of values from three independent experiments

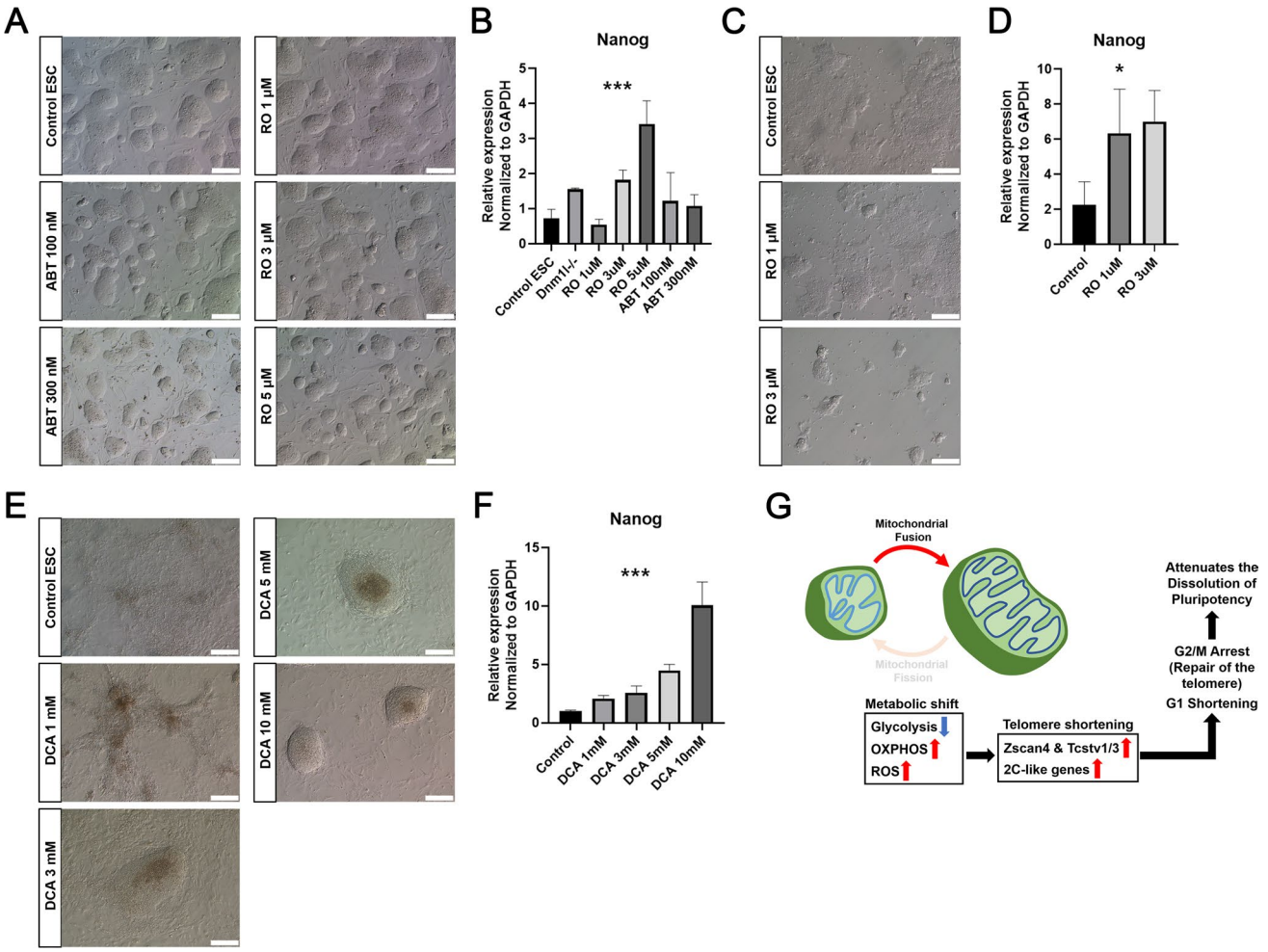

Fig. 5 Chemical-induced G2/M retardation attenuates the dissolution of pluripotency in mouse embryonic stem cells (ESCs). **A** Representative image of control ESCs observed after 3 days of cell expansion in mESC medium with RO-3306 (1, 3, and 5 µM) or ABT-751 (100 and 300 mM). Scale bars: 200 µm. **B** Real time-polymerase chain reaction (PCR) analysis for *Nanog* expression in control ESCs, *Dnm1l*$^{-/-}$ ESCs, and control ESCs treated with RO-3306 or ABT-751 for 3 days. One-way analysis of variance (ANOVA) t test: ***$p < 0.001$. Data are presented as the mean ± SEM of values from three independent experiments. **C** Representative image of control ESCs observed after 7 days of spontaneous differentiation in differentiation condition w/ or w/o RO-3306. Scale bars: 200 µm. **D** Real time-PCR analysis of Nanog in control and ESCs at day 7 of spontaneous differentiation in differentiation condition w/ or w/o RO-3306. One-way ANOVA t test: *$p < 0.05$. Data are presented as the mean ± SEM of values from three independent experiments. **E** Representative image of control ESCs observed after 7 days of spontaneous differentiation in differentiation condition w/ or w/o (dichloroacetate) DCA. Scale bars: 100 µm. **F** Real time-PCR analysis of *Nanog* in control and ESCs at day 7 of spontaneous differentiation in differentiation conditions w/ or w/o DCA. One-way ANOVA t test: ***$p < 0.001$. Data are presented as the mean ± SEM of values from three independent experiments. **G** Schematic illustration of the proposed model of *Dnm1l* deficiency-induced attenuation of the dissolution of pluripotency. *Dnm1l* deficiency in embryonic stem cells (ESCs) led to G2/M phase retardation, high levels of *Nanog* and 2-cell-specific gene expression, and metabolic shift from glycolysis to OXPHOS, which were the main causes of attenuation of the dissolution of pluripotency

undifferentiated colonies were maintained even after 7 days of differentiation induction (Fig. 5C). RO-3306 treatment groups (3 µM) maintained much higher levels of *Nanog* than those in the control, even after day 7 of differentiation (Fig. 5D). These results indicate that G2/M retardation without genetic modification can inhibit the differentiation of ESCs, which is a similar phenomenon as observed in *Dnm1l*$^{-/-}$ ESCs.

Chemically induced metabolic shift from glycolysis to OXPHOS attenuates the dissolution of pluripotency

One of the distinct phenotypes of *Dnm1l* deletion in ESCs was metabolic shift from glycolysis to OXPHOS. Hence, we tested whether chemical-induced metabolic shift without genetic modification could affect the differentiation ability

of wild-type ESCs. Dichloroacetate (DCA) is a drug that diverts metabolism from glycolysis to OXPHOS [52]. First, we determined the effect of DCA on the metabolic shift in wild-type ESCs by measuring ROS production. Wild-type ESCs were treated with DCA (1, 3, 5 and 10 mM) and ROS production was analyzed using dichlorofluorescein diacetate (DCF-DA) staining (Fig. S4B). The higher the DCA concentration, the more ROS was detected. Thereafter, we assessed the differentiation ability of DCA-treated ESCs to investigate whether the metabolism shift from glycolysis to OXPHOS could inhibit the differentiation of ESCs. Notably, DCA-treated ESCs were not differentiated; they maintained undifferentiated colonies even after 7 days of differentiation induction, indicating that metabolic shift from glycolysis to OXPHOS could attenuate the dissolution of pluripotency of ESCs (Fig. 5E). Nanog expression increased with an increase in DCA concentration (Fig. 5F). Therefore, we assumed that maintaining glycolytic metabolism in a pluripotent state or at the onset of differentiation may be required for the dissolution of pluripotency of ESCs. Given that differentiated somatic cells primarily use OXPHOS rather than glycolysis, the metabolic shift from glycolysis to OXPHOS might be a subsequent event after differentiation has progressed. Taken together, *Dnm1l* deficiency in embryonic stem cells (ESCs) led to massive changes in metabolic shift from glycolysis to OXPHOS, ROS increase, 2-cell-specific gene expression, G2/M arrest, which were the main causes of attenuation of the dissolution of pluripotency (Fig. 5G).

Global gene expression patterns of *Dnm1l*$^{-/-}$ ESCs

Lastly, RNA-seq analysis was performed to compare global gene expression patterns between control and *Dnm1l*$^{-/-}$ ESCs. At first, we performed principal component analysis (PCA) to validate sample variation and clustering as a part of quality control. PCA confirmed that the control and *Dnm1l*$^{-/-}$ ESCs were evidently separated (Fig. 6A). The volcano plot showed the differentially expressed genes ($\log_2$ |fold change|> 1.5, $p > 0.05$) between the control and *Dnm1l*$^{-/-}$ ESCs (Fig. 6B). Forty-two genes were downregulated, and sixty-nine genes were upregulated in *Dnm1l*$^{-/-}$ ESCs compared with those in control ESCs. A total of 5940 genes were further quantified using differential gene expression methods by comparing *Dnm1l*$^{-/-}$ ESCs with control ESCs ($\log_2$ |fold change|> 0) (Fig. 6C). Thereafter, we investigated the biological function of the genes differentially expressed in *Dnm1l*$^{-/-}$ ESCs compared with those in control ESCs using five bioinformatic approaches, including Gene Ontology of biological process and molecular function, Kyoto Encyclopedia of Genes and Genomes, REACTOME, and Wikipathway using Biojupies [54], a bioinformatical platform (Fig. 6D). Notably, glutathione-related terms were enriched in all categories of upregulation (Fig. 6D). We also confirmed that amino acid-related terms were enriched in four categories of downregulation, except wikipathways (Fig. S5). Therefore, the most prominent characteristic feature of *Dnm1l* deficiency in ESCs may be the functional change to reduce ROS production induced by metabolic shift.

Discussion

In this study, we demonstrated that deletion of *Dnm1l*, a mitochondrial fission-inducing gene, in ESCs caused changes in mitochondrial morphology, cellular metabolism, telomere length, ROS production, expression levels of ROS-related genes, cell cycle, and differentiation ability (dissolution of pluripotency). We focused on the mechanism of attenuation of dissolution of pluripotency via *Dnm1l* deletion. *Dnm1l*$^{-/-}$ ESCs could differentiate into three germ layers, both in vitro and in vivo; however, the size of the teratoma was smaller than that of control ESCs. Moreover, *Dnm1l*$^{-/-}$ ESCs maintained Oct4 expression and dome-like colonies even after differentiation induction for 14 days through EB formation in vitro. Here, we suggested that G2/M phase retardation, high levels of *Nanog* and differentially expressed 2-cell-specific genes, and metabolic shift from glycolysis to OXPHOS were the main causes for the inhibition of the differentiation of *Dnm1l*$^{-/-}$ ESCs.

Several studies have reported an association between Dnm1l and the G2/M phase of cell cycle. Zunino et al. showed that SENP5, a SUMO proteinase, modulates DNM1L-dependent fission during the G2/M phase [71]. We also showed that the cell cycles of *Dnm1l*$^{-/-}$ ESCs were retarded at the G2/M phase and the length of the G1 phase in *Dnm1l*$^{-/-}$ ESCs was shorter than that in control ESCs. As differentiation from ESCs primarily occur during the G1 phase [9, 42], an extended G2/M phase and a reduced G1 phase could be the cause for inhibition of the differentiation of *Dnm1l*$^{-/-}$ ESCs by reducing its time window.

It is well known that upregulation of Nanog and 2-cell-stage-specific genes affects the differentiation of ESCs [38, 46]. Practically, no changes were observed in the expression patterns of pluripotency-related genes after *Dnm1l* deletion; however, the upregulation of *Nanog* and differentially expressed 2-cell-stage-specific genes was observed, indicating that these genes could be associated with the inhibition of differentiation of *Dnm1l*$^{-/-}$ ESCs. *Nanog*-overexpressing ESCs could maintain stemness without LIF and feeder cells [20, 38], which may be a type of differentiation inhibitory effect of high levels of *Nanog*. Diego et al. suggested that less than 1% of ESC culture expressed 2-cell-stage-specific genes and these rare 2-cell-like cells show higher developmental plasticity and exit pluripotent state through a different way than that of common ESC differentiation [46]. In addition,

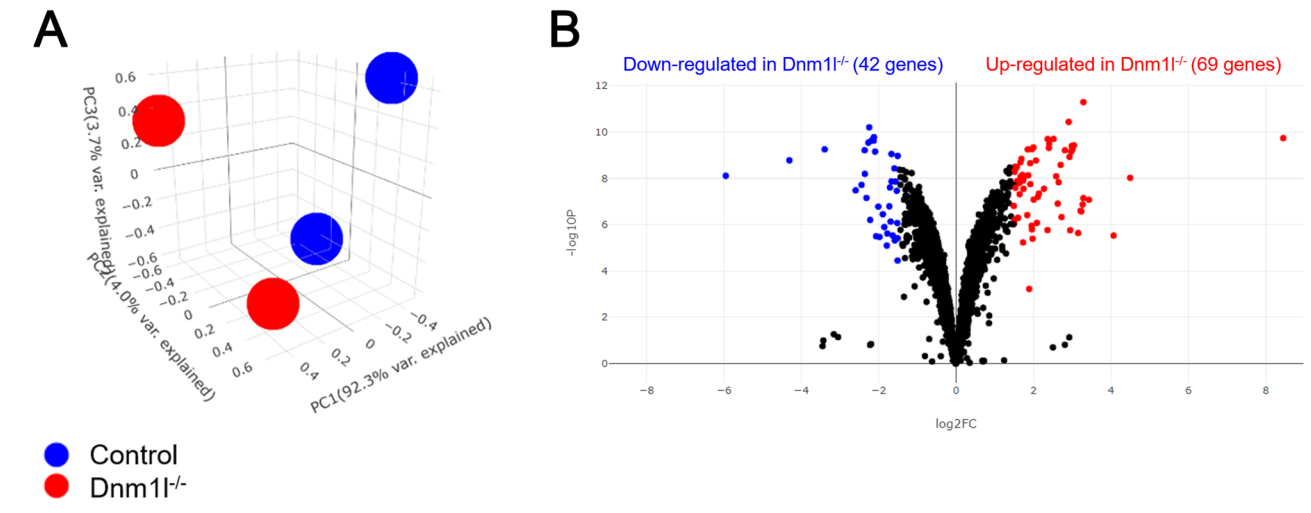

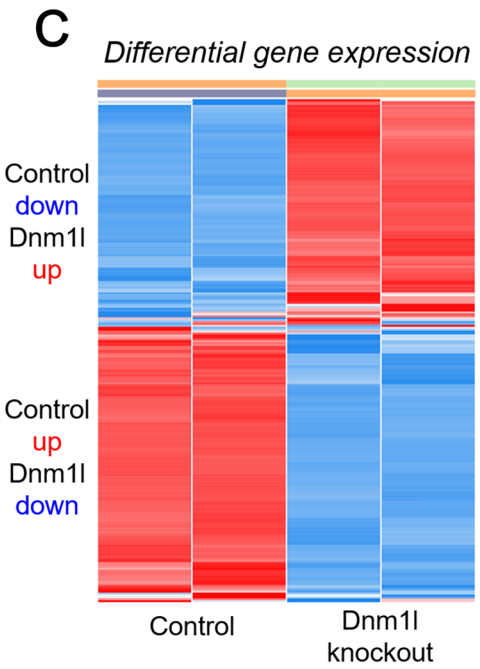

D

Up-regulated terms

	Name	pValue	TermID
GO: Biological Process	regulated exocytosis	4.72E-06	GO:0045055
	platelet degranulation	1.40E-05	GO:0002576
	regulation of cell migration	5.08E-05	GO:0030334
	regulation of fibroblast proliferation	1.35E-04	GO:0048145
	glutathione metabolic process	2.03E-04	GO:0006749
	negative regulation of sequence-specific DNA binding transcription factor activity	2.11E-04	GO:0043433
	sulfur compound biosynthetic process	0.00025	GO:0044272
	neutrophil mediated immunity	2.56E-04	GO:0002446
	purine ribonucleoside monophosphate metabolic process	0.00038	GO:0009167
	regulation of extrinsic apoptotic signaling pathway via death domain receptors	3.84E-04	GO:1902041
	Name	**pValue**	**TermID**
GO: Molecular Function	cadherin binding	1.43E-05	GO:0045296
	endoribonuclease activity	2.22E-04	GO:0004521
	protein homodimerization activity	3.30E-04	GO:0042803
	MHC class II protein complex binding	5.53E-04	GO:0023026
	MHC protein complex binding	1.11E-03	GO:0023023
	glutathione transferase activity	6.32E-03	GO:0004364
	protein kinase binding	0.00697	GO:0019901
	ribonuclease activity	7.39E-03	GO:0004540
	cytochrome-b5 reductase activity, acting on NAD(P)H	0.00875	GO:0004128
	integrin binding	9.25E-03	GO:0005178
	Name	**pValue**	**TermID**
KEGG	Glutathione metabolism	2.96E-04	hsa00480
	Metabolic pathways	3.23E-04	hsa01100
	Pathogenic Escherichia coli infection	4.21E-04	hsa05130
	Pentose phosphate pathway	6.92E-04	hsa00030
	Regulation of actin cytoskeleton	1.03E-03	hsa04810
	Proteoglycans in cancer	1.86E-03	hsa05205
	Carbon metabolism	0.00213	hsa01200
	Chronic myeloid leukemia	2.30E-03	hsa05220
	Leukocyte transendothelial migration	0.00286	hsa04670
	Bladder cancer	3.42E-03	hsa05219
	Name	**pValue**	**TermID**
REACTOME	GLI proteins bind promoters of Hh responsive genes to promote transcription	6.90E-04	R-HSA-5635851
	Metabolism	1.27E-03	R-HSA-1430728
	Extracellular matrix organization	1.76E-03	R-HSA-1474244
	Type I hemidesmosome assembly	4.43E-03	R-HSA-446107
	Platelet degranulation	5.15E-03	R-HSA-114608
	Response to elevated platelet cytosolic Ca2+	7.42E-03	R-HSA-76005
	Uptake and function of diphtheria toxin	0.00965	R-HSA-5336415
	Glutathione conjugation	1.16E-02	R-HSA-156590
	Prefoldin mediated transfer of substrate to CCT/TriC	0.01307	R-HSA-389957
	EPH-Ephrin signaling	1.79E-02	R-HSA-2682334
	Name	**pValue**	**TermID**
Wikipathway	XPodNet - protein-protein interactions in the podocyte expanded by STRING	1.62E-11	Mus musculus WP2309
	NRF2 pathway	1.51E-07	Homo sapiens WP2884
	PodNet: protein-protein interactions in the podocyte	2.25E-07	Mus musculus WP2310
	Apoptosis-related network due to altered Notch3 in ovarian cancer	4.76E-05	Homo sapiens WP2864
	Oxidative Stress	1.02E-04	Homo sapiens WP408
	IL-7 Signaling Pathway	3.36E-04	Homo sapiens WP205
	Oxidative Stress	0.00041	Mus musculus WP412
	Pathogenic Escherichia coli infection	4.21E-04	Homo sapiens WP2272
	Hedgehog Signaling Pathway	0.00055	Homo sapiens WP47
	Glutathione metabolism	7.09E-04	Mus musculus WP164

Fig. 6 RNA sequencing analysis of control and *Dnm1l*$^{-/-}$ embryonic stem cells (ESCs). **A** Principal component analysis of control and *Dnm1l*$^{-/-}$ ESCs. **B** Volcano plot analysis of control and *Dnm1l*$^{-/-}$ ESCs. **C** Clustergrammer analysis of control and *Dnm1l*$^{-/-}$ ESCs. **D** Gene ontology and pathway analyses of differentially expressed genes (DEGs) upregulated between control and *Dnm1l*$^{-/-}$ ESCs (red; glutathione related term)

ESCs expressing 2-cell-stage-specific Zscan4 express higher levels of Nanog [46], indicating that Nanog expression is correlated with Zscan4. Therefore, it will be interesting to compare the characteristics of *Dnm1l*$^{-/-}$ ESCs with 2-cell-like cells, as they share specific gene expression patterns, such as high levels of *Nanog* and 2-cell-stage-specific genes.

Metabolic shift from glycolysis to OXPHOS could be a reason for the inhibition of the differentiation of *Dnm1l*$^{-/-}$ ESCs. We showed that *Dnm1l* deletion results in an increase in ROS production via mitochondrial elongation and increased OXPHOS metabolism. Chemically induced metabolic shift from glycolysis to OXPHOS by DCA treatment could also inhibit the differentiation of ESCs. Collectively, the metabolic shift from glycolysis to OXPHOS, which is induced by Dnm1l deletion or DCA treatment, could attenuate the dissolution of pluripotency. PSCs, particularly ESCs, have globular-shaped mitochondria with immature cristae [7]. However, our results revealed that *Dnm1l*$^{-/-}$ ESCs had more elongated mitochondria and a relatively mature form of cristae compared with those of control ESCs. Notably, *Dnm1l*$^{-/-}$ ESCs showed increased levels of ROS compared to control ESCs. ROS are primarily produced in the electron transport chain [3, 27]. ROS and glycolysis inhibit each other; ROS inhibits several glycolysis-related proteins and glycolysis reduces ROS via NADPH and glutathione production [36]. Therefore, the increase in ROS production in *Dnm1l*$^{-/-}$ ESCs must be due to the changes in energy metabolism induced by elongated mitochondria. Several genes related to the Keap1-Nrf2 pathway and the SOD family, which are the major regulators of cytoprotective responses to cellular stresses [22], were also activated in *Dnm1l*$^{-/-}$ ESCs. This phenomenon might also be a counteraction against excessive ROS produced in *Dnm1l*$^{-/-}$ ESCs. In addition, considering the glycolytic function data, overall, *Dnm1l*$^{-/-}$ ESCs appear to be metabolically less active, but carry a higher spare respiratory capacity. This is probably a result of larger mitochondria or increased fusion.

One of the phenotypes of *Dnm1l*$^{-/-}$ ESCs was telomere shortening. Zscan4 is associated with telomere length [67]. Several researchers have demonstrated that Zscan4 is activated by sensing telomere shortening and subsequently facilitating telomere elongation via inhibition of DNA methylation [10, 38]. In the present study, we showed that telomere shortening and activation of Zscan4 were induced in response to *Dnm1l* deletion in ESCs. Telomere shortening can also be induced by excessive ROS levels [25, 56, 57]. Therefore, increased ROS production via mitochondrial elongation and increased OXPHOS metabolism in response to *Dnm1l* deletion may lead to telomere shortening through undefined mechanisms.

This study was performed using pluripotent mouse ESCs, which have rarely been reported for studying the relationship between mitochondrial dynamics-related genes and cellular differentiation. Among the mitochondrial dynamics-related genes, *Dnm1l* was the most effective in mitochondrial morphology and energy metabolism, and the deletion of *Dnm1l* eventually attenuated the dissolution of pluripotency. Although the mechanism is unclear, Dnm1l, as a mitochondrial fragmentation and apoptosis inducer, is associated with several diseases in humans. The unbalanced post-translational modification of Drp1 (common name of Dnm1l in humans) leads to various neurological diseases such as Alzheimer's, Huntington's, and Parkinson's diseases [1, 11, 45]. Thus, treatment with Mdivi-1, which is a well-known inhibitor of mitochondrial fission (or Drp1), is beneficial for treatment of such diseases [60]. Moreover, cardiovascular diseases are also affected by Drp1-mediated mitochondrial dynamics [35]. According to our current data, it is possible that these Drp1-related human diseases may be due to any defect in the differentiation process in the early stage of embryonic development. Further studies on Drp1 in humans need to be conducted to elucidate the etiology of neurological and cardiovascular diseases.

Supplementary Information The online version contains supplementary material available at https://doi.org/10.1007/s00018-023-04962-x.

Author contributions BJS and JTD: wrote the main manuscript and designed the study. BJS, SBN, and JC: performed experiments and analyzed data. BJS, BA, CP, KH, and JTD: performed data analysis. All authors reviewed the manuscript.

Funding This work was supported by the National Research Foundation of Korea (NRF) grant funded by the Korea government (MSIT) of the Republic of Korea (Grant No. RS-2023-00208330) and the Korea Institute of Planning and Evaluation for Technology in Food, Agriculture and Forestry (IPET), funded by the Ministry of Agriculture, Food and Rural Affairs (MAFRA) (Grant No. 322006-05-02-CG000).

Availability of data and material Data will be available on reasonable request.

Declarations

Conflict of interest The authors declare that they have no conflicts of interest.

Ethics approval and consent to participate Experiments were performed following the approved guidelines and all experimental protocols were approved by the Institutional Animal Care and Use Committee (IACUC) of Konkuk University.

Consent for publication Not applicable.

References

1. Baek SH, Park SJ, Jeong JI et al (2017) Inhibition of Drp1 ameliorates synaptic depression, Aβ deposition, and cognitive impairment in an Alzheimer's disease model. J Neurosci 37:5099–5110
2. Boroviak T, Loos R, Bertone P et al (2014) The ability of inner-cell-mass cells to self-renew as embryonic stem cells is acquired following epiblast specification. Nat Cell Biol 16:513–525
3. Brand MD (2010) The sites and topology of mitochondrial superoxide production. Exp Gerontol 45:466–472
4. Chan DC (2012) Fusion and fission: interlinked processes critical for mitochondrial health. Annu Rev Genet 46:265–287
5. Chang DT, Honick AS, Reynolds IJ (2006) Mitochondrial trafficking to synapses in cultured primary cortical neurons. J Neurosci 26:7035–7045

6. Choi HW, Joo JY, Hong YJ et al (2016) Distinct enhancer activity of Oct4 in naive and primed mouse pluripotency. Stem Cell Rep 7:911–926
7. Choi J, Seo BJ, La H et al (2020) Comparative analysis of the mitochondrial morphology, energy metabolism, and gene expression signatures in three types of blastocyst-derived stem cells. Redox Biol 30:101437
8. Chung S, Arrell DK, Faustino RS et al (2010) Glycolytic network restructuring integral to the energetics of embryonic stem cell cardiac differentiation. J Mol Cell Cardiol 48:725–734
9. Coronado D, Godet M, Bourillot P-Y et al (2013) A short G1 phase is an intrinsic determinant of naive embryonic stem cell pluripotency. Stem Cell Res 10:118–131
10. Dan J, Rousseau P, Hardikar S et al (2017) Zscan4 inhibits maintenance DNA methylation to facilitate telomere elongation in mouse embryonic stem cells. Cell Rep 20:1936–1949
11. Devoto VMP, Falzone TL (2017) Mitochondrial dynamics in Parkinson's disease: a role for α-synuclein? Dis Model Mech 10:1075–1087
12. Evans MJ, Kaufman MH (1981) Establishment in culture of pluripotential cells from mouse embryos. Nature 292:154–156
13. Facucho-Oliveira J, John JS (2009) The relationship between pluripotency and mitochondrial DNA proliferation during early embryo development and embryonic stem cell differentiation. Stem Cell Rev Rep 5:140–158
14. Facucho-Oliveira JM, Alderson J, Spikings EC et al (2007) Mitochondrial DNA replication during differentiation of murine embryonic stem cells. J Cell Sci 120:4025–4034
15. Ferguson SM, De Camilli P (2012) Dynamin, a membrane-remodelling GTPase. Nat Rev Mol Cell Biol 13:75–88
16. Folmes CD, Dzeja PP, Nelson TJ et al (2012) Metabolic plasticity in stem cell homeostasis and differentiation. Cell Stem Cell 11:596–606
17. Folmes CD, Nelson TJ, Martinez-Fernandez A et al (2011) Somatic oxidative bioenergetics transitions into pluripotency-dependent glycolysis to facilitate nuclear reprogramming. Cell Metab 14:264–271
18. Giacomello M, Pyakurel A, Glytsou C et al (2020) The cell biology of mitochondrial membrane dynamics. Nat Rev Mol Cell Biol 21:204–224
19. Hanahan D, Weinberg RA (2011) Hallmarks of cancer: the next generation. Cell 144:646–674
20. Heurtier V, Owens N, Gonzalez I et al (2019) The molecular logic of Nanog-induced self-renewal in mouse embryonic stem cells. Nat Commun 10:1–15
21. Ishihara N, Nomura M, Jofuku A et al (2009) Mitochondrial fission factor Drp1 is essential for embryonic development and synapse formation in mice. Nat Cell Biol 11:958–966
22. Kansanen E, Kuosmanen SM, Leinonen H et al (2013) The Keap1-Nrf2 pathway: mechanisms of activation and dysregulation in cancer. Redox Biol 1:45–49
23. Kasai S, Shimizu S, Tatara Y et al (2020) Regulation of Nrf2 by mitochondrial reactive oxygen species in physiology and pathology. Biomolecules 10:320
24. Kauffman ME, Kauffman MK, Traore K et al (2016) MitoSOX-based flow cytometry for detecting mitochondrial ROS. React Oxyg Species (Apex, NC) 2:361
25. Ko E, Seo HW, Jung G (2018) Telomere length and reactive oxygen species levels are positively associated with a high risk of mortality and recurrence in hepatocellular carcinoma. Hepatology 67:1378–1391
26. Kondoh H, Lleonart ME, Nakashima Y et al (2007) A high glycolytic flux supports the proliferative potential of murine embryonic stem cells. Antioxid Redox Signal 9:293–299
27. Kowaltowski AJ, De Souza-Pinto NC, Castilho RF et al (2009) Mitochondria and reactive oxygen species. Free Radical Biol Med 47:333–343
28. Lapasset L, Milhavet O, Prieur A et al (2011) Rejuvenating senescent and centenarian human cells by reprogramming through the pluripotent state. Genes Dev 25:2248–2253
29. Li Z, Okamoto K-I, Hayashi Y et al (2004) The importance of dendritic mitochondria in the morphogenesis and plasticity of spines and synapses. Cell 119:873–887
30. Lonergan T, Bavister B, Brenner C (2007) Mitochondria in stem cells. Mitochondrion 7:289–296
31. Ma Q (2013) Role of nrf2 in oxidative stress and toxicity. Annu Rev Pharmacol Toxicol 53:401–426
32. Mandal S, Freije WA, Guptan P et al (2010) Metabolic control of G1–S transition: cyclin E degradation by p53-induced activation of the ubiquitin–proteasome system. J Cell Biol 188:473–479
33. Martello G, Smith A (2014) The nature of embryonic stem cells. Annu Rev Cell Dev Biol 30:647–675
34. Mitra K, Wunder C, Roysam B et al (2009) A hyperfused mitochondrial state achieved at G1–S regulates cyclin E buildup and entry into S phase. Proc Natl Acad Sci 106:11960–11965
35. Morales PE, Arias-Durán C, Ãvalos-Guajardo Y et al (2020) Emerging role of mitophagy in cardiovascular physiology and pathology. Mol Aspects Med 71:100822
36. Mullarky E, Cantley LC (2015) Diverting glycolysis to combat oxidative stress. Innov Med. 3–23
37. Murnane JP (2012) Telomere dysfunction and chromosome instability. Mutat Res Fundam Mol Mech Mutagen 730:28–36
38. Nakai-Futatsugi Y, Niwa H (2016) Zscan4 is activated after telomere shortening in mouse embryonic stem cells. Stem Cell Rep 6:483–495
39. Namani A, Rahaman MM, Chen M et al (2018) Gene-expression signature regulated by the KEAP1-NRF2-CUL3 axis is associated with a poor prognosis in head and neck squamous cell cancer. BMC Cancer 18:46
40. Oliver D, Reddy PH (2019) Dynamics of Dynamin-related protein 1 in Alzheimer's disease and other neurodegenerative diseases. Cells 8:961
41. Otera H, Ishihara N, Mihara K (2013) New insights into the function and regulation of mitochondrial fission. Biochim Biophys Acta (BBA) Mol Cell Res 1833:1256–1268
42. Pauklin S, Vallier L (2013) The cell-cycle state of stem cells determines cell fate propensity. Cell 155:135–147
43. Qian W, Choi S, Gibson GA et al (2012) Mitochondrial hyperfusion induced by loss of the fission protein Drp1 causes ATM-dependent G2/M arrest and aneuploidy through DNA replication stress. J Cell Sci 125:5745–5757
44. Ran FA, Hsu PD, Wright J et al (2013) Genome engineering using the CRISPR-Cas9 system. Nat Protoc 8:2281
45. Reddy PH (2009) Amyloid beta, mitochondrial structural and functional dynamics in Alzheimer's disease. Exp Neurol 218:286–292
46. Rodriguez-Terrones D, Gaume X, Ishiuchi T et al (2018) A molecular roadmap for the emergence of early-embryonic-like cells in culture. Nat Genet 50:106–119
47. Salazar-Roa M, Malumbres M (2017) Fueling the cell division cycle. Trends Cell Biol 27:69–81
48. Seo BJ, Choi J, La H et al (2020) Role of mitochondrial fission-related genes in mitochondrial morphology and energy metabolism in mouse embryonic stem cells. Redox Biol 36:101599
49. Seo BJ, Yoon SH, Do JT (2018) Mitochondrial dynamics in stem cells and differentiation. Int J Mol Sci 19:3893
50. Song M, Mihara K, Chen Y et al (2015) Mitochondrial fission and fusion factors reciprocally orchestrate mitophagic culling in mouse hearts and cultured fibroblasts. Cell Metab 21:273–286

51. Taguchi N, Ishihara N, Jofuku A et al (2007) Mitotic phosphorylation of dynamin-related GTPase Drp1 participates in mitochondrial fission. J Biol Chem 282:11521–11529
52. Tataranni T, Agriesti F, Pacelli C et al (2019) Dichloroacetate affects mitochondrial function and stemness-associated properties in pancreatic cancer cell lines. Cells 8:478
53. Tonelli C, Chio IIC, Tuveson DA (2018) Transcriptional regulation by Nrf2. Antioxid Redox Signal 29:1727–1745
54. Torre D, Lachmann A, Maayan A (2018) BioJupies: automated generation of interactive notebooks for RNA-Seq data analysis in the cloud. Cell Syst 7:556-561 e553
55. Vardhana SA, Arnold PK, Rosen BP et al (2019) Glutamine independence is a selectable feature of pluripotent stem cells. Nat Metab 1:676–687
56. Von Zglinicki T (2002) Oxidative stress shortens telomeres. Trends Biochem Sci 27:339–344
57. Von Zglinicki T, Saretzki G, Döcke W et al (1995) Mild hyperoxia shortens telomeres and inhibits proliferation of fibroblasts: a model for senescence? Exp Cell Res 220:186–193
58. Wai T, Langer T (2016) Mitochondrial dynamics and metabolic regulation. Trends Endocrinol Metab 27:105–117
59. Wakabayashi J, Zhang Z, Wakabayashi N et al (2009) The dynamin-related GTPase Drp1 is required for embryonic and brain development in mice. J Cell Biol 186:805–816
60. Wang W, Yin J, Ma X et al (2017) Inhibition of mitochondrial fragmentation protects against Alzheimer's disease in rodent model. Hum Mol Genet 26:4118–4131
61. Westermann B (2010) Mitochondrial fusion and fission in cell life and death. Nat Rev Mol Cell Biol 11:872–884
62. White J, Dalton S (2005) Cell cycle control of embryonic stem cells. Stem Cell Rev 1:131–138
63. Xu X, Duan S, Yi F et al (2013) Mitochondrial regulation in pluripotent stem cells. Cell Metab 18:325–332
64. Yang J, Guo R, Wang H et al (2016) Tet enzymes regulate telomere maintenance and chromosomal stability of mouse ESCs. Cell Rep 15:1809–1821
65. Yeh CD, Richardson CD, Corn JE (2019) Advances in genome editing through control of DNA repair pathways. Nat Cell Biol 21:1468–1478
66. Ying Q-L, Smith AG (2003) Defined conditions for neural commitment and differentiation. Methods Enzymol 365:327–341
67. Zalzman M, Falco G, Sharova LV et al (2010) Zscan4 regulates telomere elongation and genomic stability in ES cells. Nature 464:858–863
68. Zhang J, Nuebel E, Daley GQ et al (2012) Metabolic regulation in pluripotent stem cells during reprogramming and self-renewal. Cell Stem Cell 11:589–595
69. Zhang Q, Dan J, Wang H et al (2016) Tcstv1 and Tcstv3 elongate telomeres of mouse ES cells. Sci Rep 6:19852
70. Zhou W, Choi M, Margineantu D et al (2012) HIF1α induced switch from bivalent to exclusively glycolytic metabolism during ESC-to-EpiSC/hESC transition. EMBO J 31:2103–2116
71. Zunino R, Braschi E, Xu L et al (2009) Translocation of SenP5 from the nucleoli to the mitochondria modulates DRP1-dependent fission during mitosis. J Biol Chem 284:17783–17795